THE ASTROPHYSICAL JOURNAL, 560:490–498, 2001 October 10

SOLAR POLAR PLUME LIFETIME AND CORONAL HOLE EXPANSION: DETERMINATION FROM LONG-TERM OBSERVATIONS

C. E. DEFOREST[1]
Southwest Research Institute, 1050 Walnut Street Box 426, Boulder, CO 80302; deforest@boulder.swri.edu
AND
P. L. LAMY AND A. LLEBARIA
Laboratoire d'Astronomie Spatiale (CNRS), Traverse du Siphon, Les Trois Lucs, Marseille, F-13012, France
Received 2001 March 23; accepted 2001 June 12

ABSTRACT

We have generated off-limb polar synoptic charts of polar plume evolution at various solar altitudes using EUV Imaging Telescope and Large Angle and Spectrometric Coronagraph data from 1996 December. The charts allow direct measurement of the altitude expansion of the solar minimum coronal holes. We find expansion values that are consistent with the conventional picture of superradial expansion and inconsistent with radial expansion. Using visible red line data as a bridge between EUV and white-light images of the corona, we are able to confirm that the coronal structure seen at the base of the corona is preserved throughout the considered altitude range of 1.1–3.0 $R_{\odot}$. We show that polar plumes are episodic in nature, lasting perhaps 24 hr but recurring for up to weeks at a time; this strengthens the picture that they are caused by magnetic heating under the influence of supergranulation.

Subject headings: solar wind — Sun: activity — Sun: corona — techniques: image processing

1. INTRODUCTION

Polar plumes are dense, relatively cool, magnetically open linear structures in the solar corona. They arise from within the polar coronal holes that exist near solar minimum, from nearly unipolar magnetic footpoints, and expand to altitudes of over 30 $R_{\odot}$ (DeForest et al. 1997; DeForest, Plunkett, & Andrews 2001). Although plumes are probably not the principal source of the high-speed solar wind (Wang 1994; Hassler et al. 1999; Banerjee et al. 2000; Cranmer et al. 1999; Giordano et al. 2000), they must interact with the main wind somewhere between 30 $R_{\odot}$ and 1 AU because they are not seen by in situ instruments on *Ulysses* (McComas et al. 1995; Poletto et al. 1996; Reisenfeld, McComas, & Steinberg 1999).

Polar plumes and coronal rays are related structures that are defined observationally. Rays have been defined as linear, approximately radial structures visible in white light, while polar plumes are associated with a particular morphology on the solar surface. Most rays can be associated directly with plumes on the solar surface (DeForest et al. 2001), while the very brightest are associated with the high-density structures at lower latitudes (Li, Jewitt, & Labonte 2000a; Li et al. 2000b). Rays were first observationally associated with magnetic flux concentrations by Saito (1965), and several authors since then have associated them with unipolar flux concentrations in the supergranular network boundaries (Newkirk & Harvey 1968; Fisher & Guhathakurta 1995; DeForest et al. 1997). At least in the lower corona, plumes have $\beta < 1$ and hence trace the lines of an approximately force-free field that extends through the coronal hole. Hence, plumes and other bright structures in the hole may be considered as tracers of the field as a whole.

Coronal holes and the structures within them have long been thought to expand superradially with altitude (Munro & Jackson 1977; Fisher & Guhathakurta 1995) in the lower corona; this geometry affects profoundly our understanding of the origin and acceleration mechanism of the high-speed solar wind. The high-speed solar wind at even moderate solar latitudes is thought to originate within coronal holes at high latitude and to be affected by the "nozzling" effect of the superradial expansion (Zirker 1977). Several recent papers purport to observe a radial, rather than superradial, morphology in coronal holes (Woo & Habbal 1999; Woo et al. 1999), challenging this conventional understanding. The arguments to date for radial or superradial expansion hinge mostly on the interpretation of individual images or single digital montages and hence are subject to ambiguity: different people may look at the same image and see different things. We present a more objective way than direct image observation to observe the expansion rate of coronal holes, taking advantage of the structures within the holes as tracers. We both trace individual structures and also determine the holistic degree of matching across the whole coronal hole through cross-correlation analysis. Our results support a conventional picture of coherently expanding coronal holes, with significant superradial expansion between the surface of the Sun and the midcorona at 2–3 $R_{\odot}$.

It has been suggested (Saito 1965; Wang 1998) that plumes are heated by reconnection between small magnetic bipoles and larger unipolar flux concentrations in the supergranular network. If plumes are actually powered by magnetic reconnection on this scale, they should have timescales similar to that of supergranular turnover ($\sim$1 day), which is consistent with the $\sim$8–20 hr timescale derived from EUV Imaging Telescope (EIT) time sequence studies. However, the large number of plumes in the EIT field of view may cause individual plumes to be lost in the general "forest" after only a few hours, and studies that look for individual plumes at widely separated times have found that plumes may last for up to 2 weeks (Withbroe, Feldman, & Ahluwalia 1991). Using a month-long time series of EIT images (Delaboundinière et al. 1995), we have determined that

[1] Much of this work was performed in affiliation with Stanford University.

polar plumes are both transient and persistent: they are recurring structures that brighten for only ~ 1 day but reappear at approximately the same location for up to 2 weeks. This temporal behavior is consistent with single large unipolar flux concentrations encountering multiple ephemeral dipoles under the influence of supergranulation, suggesting that polar plumes are indeed the results of small-scale magnetic reconnection that is driven by supergranular motion.

In earlier work, we have generated off-limb "time intensity diagrams" of coronal brightness, measured by the Large Angle and Spectrometric Coronograph Experiment (LASCO) C-2 at a particular sky plane altitude, versus time and near-polar azimuthal angle (colatitude; Lamy et al. 1997; Llebaria et al. 1998). Recently, Li et al. (2000a) used similar diagrams to demonstrate that the very brightest coronal rays are associated with the passage of active regions and associated streamers across the disk by finding the rigid-body rotation curves that best match the rays' passage through the diagram.

Figure 1 demonstrates the construction of a typical time intensity diagram in a coronal hole; conceptually, a time sequence of images is stacked in order, and a curved slice is cut through all images. The image formed by the brightness values on the two-dimensional manifold of the cut forms the time intensity diagram. Time intensity diagrams give insight into the lifetimes of individual coronal structures because they record the evolution of rigid, extended objects as identifiable spatial structures. Diagrams taken near the equator form coronal off-limb synoptic charts that are commonly used to understand the structure of the global corona.

Because the solar rotation sweeps each part of the corona across different azimuthal angles, time intensity diagrams taken near the poles form "sinograms" of the Sun's rotation. Sinograms, named for the sine waves traced by individual features, are used for tomography of optically thin objects. Solar rotation coronal sinograms are not directly useful for small-scale tomography because the coronal structures evolve on time scales faster than the solar rotation rate, but a rotation sinogram does encode a unique signature of the cross-sectional evolution of the coronal hole at one altitude. Comparing sinograms made at the same time with different instruments or at different altitudes summarizes the spatial correspondence between all features that are visible to each instrument at each altitude. Because plumes are linear features that extend from the surface through all altitudes in the lower corona, an individual plume may be expected to be visible in simultaneous sinograms from all altitudes. Our early comparisons between simultaneous sinograms made with EIT at 1.1 $R_{\odot}$ and with LASCO C-2 at 2 $R_{\odot}$ showed poor to nonexistent correspondence (Llebaria et al. 1998), leading to initial speculation that the plumes viewed with EIT were not the same objects as the rays observed with C-2.

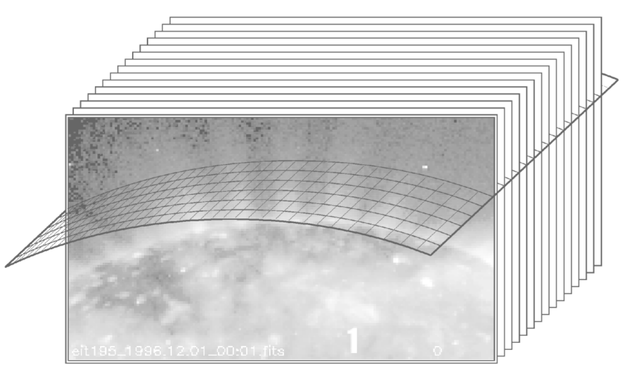

FIG. 1.—Construction of a "sinogram" (polar time-intensity diagram) from a sequence of coronal images. Notionally, a time sequence of images is stacked and then sliced along a curve that is concentric with the disk center, yielding an image whose horizontal coordinate is azimuth and whose vertical coordinate is time. Study of individual sinograms yields insight into coronal evolution. Comparison between sinograms made at different altitudes shows how the coronal structure varies with altitude.

In the present work, we carefully compare four different types of sinograms made with EIT, LASCO C-1, and LASCO C-2 at several altitudes during the month of 1996 December and explore the results that can be gleaned from the comparison. We find that polar plumes are episodic in nature, recurring in approximately the same location for up to 3 weeks at a time, that the plumes observed with white-light coronagraphs such as LASCO are indeed the same structures as those observed with EUV instruments such as EIT, and that the coronal hole undergoes approximately uniform superradial expansion consistent with expansion factors similar to those quoted by earlier authors.

2. OBSERVATIONS AND DATA PREPARATION

The month of 1996 December was the first month in which EIT recorded high-cadence "coronal mass ejection watch" synoptic full-field images of the Sun in its 195 Å (Fe XII; $\sim 1.5 \times 10^6$ K) band. The images were recorded approximately once every 18 minutes throughout the month. The northern polar coronal hole was particularly well defined that month, and every day there were several bright plumes visible. Also, throughout most of that month, several LASCO C-1 and C-2 exposures were recorded each day. During the week of December 21–27, LASCO C-1 was shut down, and EIT entered a lower rate mode of observing, so that C-2 and C-3 could record images at much higher cadence. Figure 2 shows sample exposures in each of four observing bands: EIT 195 Å, the LASCO C-1 6376 Å "red line" (the 6376 Å passband includes the Fe X line at 6374 Å), the LASCO C-1 6380 Å "red continuum," and LASCO C-2 orange light.

All four channels of data required conditioning before they could be used. Because EIT and LASCO share the same on-board computer and control electronics, some of the steps required are the same for each instrument. All the images were initially scaled to the same 512×512 pixel size, then normalized for actual exposure time. Missing data were replaced with data from adjacent images in the time series. LASCO C-1 and C-2 data were despiked using an unsharp-masking spike detection algorithm and then background-subtracted using techniques specific to each channel. The C-2 background model was the standard model prepared at the Naval Research Laboratory (NRL) as in Wu et al. (1997). The C-1 line images at 6376 Å were background-subtracted using the adjacent 6380 Å images as background sources, as in Brueckner et al. (1995). Unsharp masking removed the background from the C-1 continuum images.

The final image sequences were transformed into azimuthal coordinates (in which the radial direction is vertical and the azimuthal direction is horizontal). The resulting data sets had three independent variables: azimuth, radius, and time. A slice through each data set across the radial

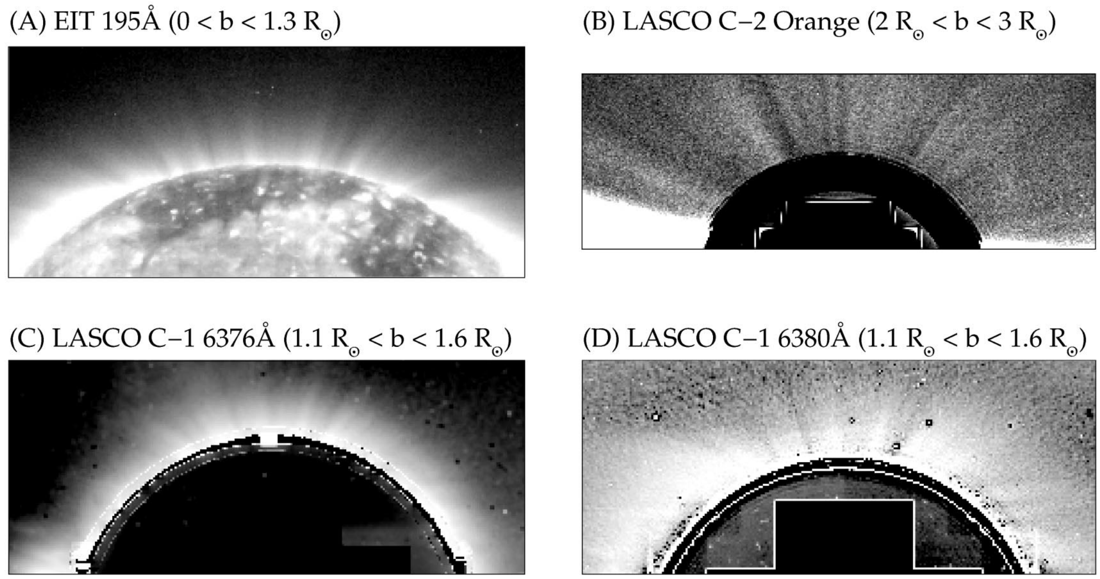

FIG. 2.—Sample observations of plumes from three instruments aboard *SOHO* during the observation period in 1996 December. The northern coronal hole was particularly well formed, and several bright plumes were visible. (*a*) *SOHO*/EIT image at 195 Å (Fe XII; 1.5×10^6 K). (*b*) LASCO C-2 orange-filter broadband visible image (Thomson scattered light). (*c*) LASCO C-1 coronal red line image in the 6376 Å channel (Fe X; 1×10^6 K). (*d*) LASCO C-1 visible continuum image in the 6380 Å channel (Thomson-scattered light). The C2 altitude range was limited by cropping of the northern and southern edges of the images in the 1996 synoptic program. The C1 altitude range was limited by S/N characteristics of the images.

direction yields a sinogram: an image of intensity versus azimuth and time at a particular altitude. The azimuthal pixel scale of each data cube was chosen to suit that instrument's azimuthal resolution.

The C-1 data required special care in preparation because the background-subtraction steps could not remove all of the scattered light and other artifacts from the images (and the continuum images were not background-subtracted at all). We unsharp-masked the C-1 data by convolving them with a plus-sign–shaped kernel and subtracting the convolved image from the original. This step removes both all localized but stationary features and all coherent global variations in intensity. For consistency, both the EIT and the C-2 data were treated the same way so that the images could be compared.

Figure 3 shows sinograms from representative altitudes in each of the four data products. The horizontal scale varies from instrument to instrument to match the super-radial expansion of the corona with altitude. The large horizontal gap near the top of the C-1 sinograms marks the period when no C-1 data were recorded. Some residual spikes survived the C-1 continuum despiking process; the plus sign–shaped unsharp masking kernel is apparent around each of these spikes in the figure. The EIT and C-2 images have much higher signal-to-noise ratios (S/Ns) than the C-1 images, mostly because the C-1 images are heavily background-subtracted.

3. ANALYSIS AND DISCUSSION

3.1. *Plume Lifetime*

The sinogram in Figure 3*a* represents 60° of azimuth, 30° on each side of the pole. Polar plumes may be seen as diagonal tracks, several of which are marked. Plumes in the foreground travel from left to right with the Sun's rotation, forming tracks that are slanted up and to the right. Plumes behind the Sun are also visible because of the corona's optically thin character. They form tracks that are slanted up and to the left and are typically somewhat dimmer than the foreground plumes because the EUV optical density of the corona is both nonzero and small. Typical brightenings last anywhere from 0.5 to 2 days. The edges of the field of view are marked by exceptionally bright and dark blotches; these are the edges of the coronal hole and associated artifacts due to the unsharp masking and the irregular shape of the coronal hole. The lower vertical resolution near the top of the image is due to a 2 day period in which EIT collected only one image per day, during the week-long Christmas movie sequence.

The blobby character of the EIT sinogram shows that plumes have a short lifetime, but the existence of perceptible tracks that extend over periods of up to 3 weeks (two such tracks are identified in the figure) indicates that they are recurrent in approximately the same location for long periods. The blobs in Figure 1 are not merely due to two-plume coincidences in the rotation; they are typically more than twice as bright as each of the surrounding pixels.

The recurrent nature of plumes together with the observation that plume footpoints always correspond to magnetic flux concentrations are surprising because the supergranulation is commonly thought to dissociate flux concentrations on a timescale of only a few times 24 hr. The plume tracks in Figure 1 follow anomalous rotation curves; the derived solar rotation period varies from 6 weeks to 8 days.

The persistence of flux concentrations is evidence of deep structure in the magnetic field. The process of flux motion on the surface is commonly considered as a random walk under the influence of granulation and supergranulation. Such a random walk disperses flux but does not eradicate it, so that one is more likely to find flux concentrations near the sites of old ones than in randomly chosen places on the Sun. However, the anomalous rotation rates of the longer plume tracks in Figure 1 last too long to be consistent with random motions such as that picture would suggest. The larger plume sites appear to undergo coherent motion rela-

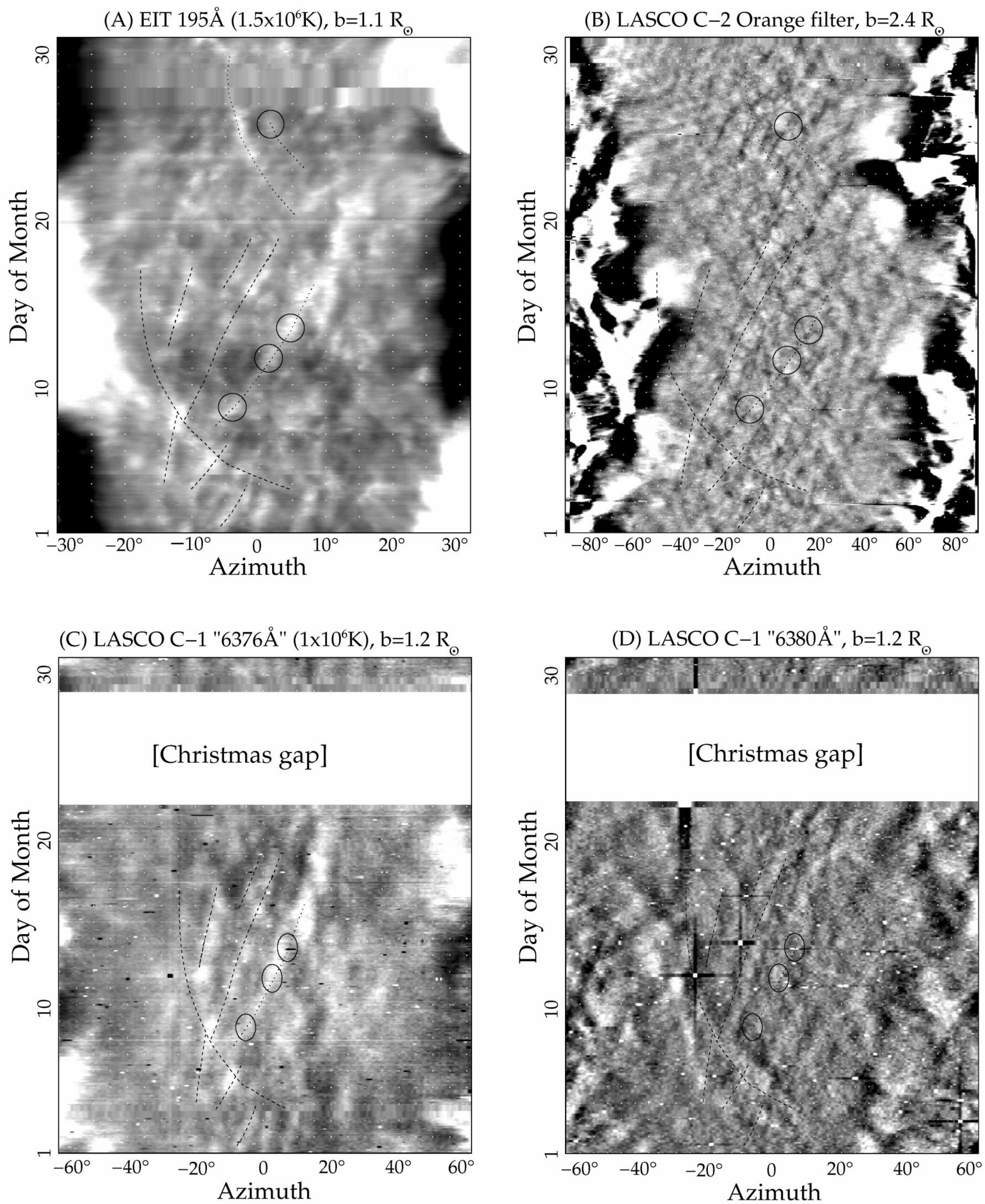

FIG. 3.—Sinograms for 1996 December, with several instruments and at several solar altitudes. (*a*) EIT 195 Å at 1.06 $R_\odot$. (*b*) LASCO C-2 orange filter at 2.39 $R_\odot$. (*c*) LASCO C-1 6376 Å, "red line," at 1.18 $R_\odot$. (*d*) LASCO C-1 6380 Å, "red continuum," at 1.18 $R_\odot$. Note the similarities between the two collisionally excited (EIT and C-1 6376 Å) channels and between the two scattered light (C-2 and C-1 6380 Å) channels. See text for more discussion of the features.

tive to the corotating frame, suggesting that some subsurface coherent magnetic structure is at play. The plume sites' lifetime is on the order of 10 days, $\sim$10 supergranulation times.

The intermittent pattern of plume lifetime supports the theory that magnetic reconnection in the supergranular network lanes is responsible for plume formation, as has been suggested based on studies of co-aligned magnetic and EUV emission data (Wang & Sheeley 1995; DeForest et al. 1997; Wang 1998), because the timescale of the stochastic brightening is approximately equal to the timescale on which flux is recycled in the network (Schrijver et al. 1997). To determine whether stochastic scattering and regathering of flux or similar network driven processes are sufficient to explain the plumes' appearance and disappearance, more work is needed on both the statistics and detailed evolution of high-latitude flux concentrations.

3.2. *Identification of Structures across Altitudes*

It is difficult to associate directly visible-light coronal rays in the mid- to outer corona with individual EUV plumes at the solar surface. The difficulties arise from emission physics differences between the visible light used by broadband coronagraphs and the EUV used to image the lowest strata of the corona, and also from the current lack of a low-noise coronagraph that encompasses the altitude range from 1.5 to 2.0 $R_{\odot}$. The emission physics effects change the apparent relative brightness and structure of the plumes, while the lack of intermediate altitude coverage prevents direct association of structures by proximity.

The C-1 sinograms shown in Figure 3 provide a bridge between the EUV low-altitude measurements from EIT and the scattered light high-altitude measurements from C-2; C-1 measures both collisionally excited and scattered light from the same altitude range, allowing the separation of the effects of the different measurement from the effects of altitude.

Each panel in Figure 3 has several linelike and pointlike features marked. The features were hand-traced over the EIT sinogram, and the traced pattern was scaled as a unit to match the observed horizontal scale of each of the other images. The C-1 red line and C-1 continuum patterns are at the same altitude and scale. There is good correspondence between features in the three low-altitude (EIT, C-1 red line, and C-1 continuum) images and fair correspondence between the C-1 continuum and high-altitude (C-2) images, although the relative brightnesses of the features vary significantly between images. With guidance from the "landmark" figures drawn on the image, the eye picks out many other features that correspond between the EUV and C-2 images in Figures 3*a* and 3*b*. In particular, most bright features that are visible in any of the four frames correspond to similarly placed features in each of the other images. The relative intensities of features are similar between Figures 3*a* and 3*c* and between Figures 3*b* and 3*d*, showing qualitatively that the gross differences in the type of measurement account for much of the apparent difference between the features in Figures 3*a* and 3*b*.

The positional mismatches between the features in Figures 3*a* and 3*b* are largely due to the imperfect homogeneity of the expansion. For example, the line with three circled features matches its plume track well at 1.1–1.2 $R_{\odot}$, but at 2.4 $R_{\odot}$, its slope and azimuth do not match perfectly. The other traces are, in general, slightly displaced as well in the C-2 image. The trend is that features that are close to the pole do not expand as much as features far from the pole, suggesting that the coronal hole's expansion is only approximately uniform. Such a trend toward lower expansion near the center of the coronal hole is also to be expected from magnetic models of the coronal holes (see, e.g., Suess et al. 1998) because of the propagation of magnetic pressure across the field lines.

3.3. *Cross-Altitude Comparisons*

To eliminate the inherent subjectivity of visual inspection, we measured the cross-correlation coefficient of sinograms made with different instruments and at different altitudes. Cross-altitude correlation between images generates a holistic measurement both of how rapidly the coronal hole expands and also of how well the overall shape is preserved against altitude and different forms of detection. Furthermore, the presence of LASCO C-1 data in the lower altitude region allows a check on the qualitative observation that the features seen above 2 $R_{\odot}$ in the C-2 data are extensions of the same features that are seen in the lower corona with EIT.

We determined the pixelwise correlation coefficient between each pair of sinograms by comparing the central portions of two images, while we varied the azimuthal scale of the inner image to maximize the correlation coefficient versus altitude. To eliminate edge effects near the hole boundaries, we compared only the innermost 50% of the scaled images (in the azimuthal direction). Plots of this type give an overall estimate of the best-fit expansion factor of the coronal hole. They also summarize information about the noise level in the instrument and about the coherence of the expansion; noise in the measurement lowers the correlation coefficient, as does differential expansion or twist of the features.

Figure 4 shows a plot of the cross-correlation coefficient versus the superradial expansion factor and altitude across sinograms at several representative altitudes in each instrument. Each plotted line represents the total correlation coefficient between sinograms at the two stated altitudes plotted versus linear horizontal compression of the upper sinogram. In general, sinograms at higher altitudes have correlation maxima at larger scale factors, reflecting the superradial expansion of the coronal hole.

Figure 4*a* shows the correlation coefficient versus the expansion factor and altitude for EIT images in the lower corona. The tallest peak represents correlation of the 1.06 $R_{\odot}$ sinogram with itself; it reaches 1 at a scale factor of 1. The solid line, at 0.98 $R_{\odot}$, shows that the corona is optically thin: the peak correlation is only ~ 0.5 because only approximately half of the structures visible at 1.06 $R_{\odot}$ are in front of the limb and visible at 0.98 $R_{\odot}$. Noise is negligible at 1.06 $R_{\odot}$ with this instrument, as evidenced by the peak heights of 0.9 for 1.02 and 1.10 $R_{\odot}$, which have the curves on either side of the referent altitude of 1.06 $R_{\odot}$. The graphs dip below zero because of the unsharp masking; pixels at intermediate distances from a central point are anticorrelated with the center because the masking kernel is negative at intermediate distances. When the scale factor causes enough positional mismatch between the stretched images, this coherent effect dominates the absolute correlation coefficient.

The LASCO C-2 plots in Figure 4*b* appear broadly similar to the EIT plots in Figure 4*a*. Both the EIT and LASCO data show coherent structures that rotate over several days. The somewhat narrower width of the central peaks in the white light is due to the finer structure that dominates the C-2 sinograms; while the EIT sinograms, with their n_e^2 brightness dependence, are dominated by the few densest visible structures structures, the C-2 sinograms are sensitive to finer details in the overall background structure.

The C-1 plots in Figures 4*c* and 4*d* show much stronger effects from background noise than do Figures 4*a* and 4*b*, reflecting the lower S/N of those images. In particular, the negative-valued troughs are smoothed nearly completely away in both sets of C-1 plots because the negative coherent effect from unsharp masking is well below the noise floor of each image. The red-line correlation coefficients drop off rapidly as the line brightness fades with altitude. Figure 4*d* shows that the continuum images have S/Ns on the order of unity: even small-scale factors misalign uncorrelated noise in the copies of the sinogram at 1.18 $R_{\odot}$, rapidly reducing the correlation coefficient from 1.0 to ~ 0.6 in the control curve. Hence, the S/N is at most ~ 2 at this altitude. However, identifiable peaks still show a nice expansion profile out to the highest plotted altitude at 1.6 $R_{\odot}$.

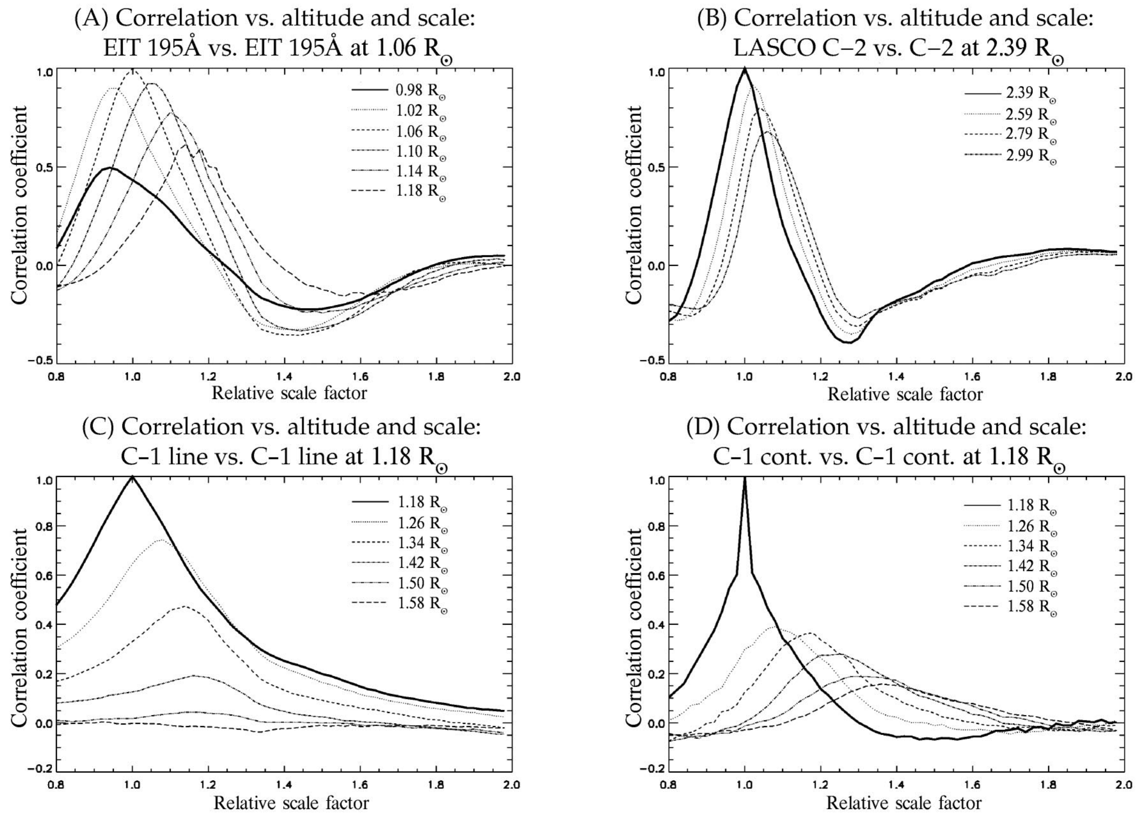

FIG. 4.—Sinogram cross-correlation coefficients across altitude and horizontal scaling (superradial expansion factor) for each of the data sets shown in Fig. 3. Sinograms are compared in pairs; a reference sinogram is expanded horizontally by the relative scale factor, and the pixelwise correlation coefficient with some other sinogram is plotted. The peak correlation coefficients drop with altitude primarily because of the lower S/N at higher altitudes. No radial component to the coronal hole (with scale factor 1.0) is seen in any of these altitude ranges.

3.4. *Coherent Expansion*

The peak correlation coefficients in Figure 4 drop with altitude because of the lower S/N at higher altitudes. Spatial decoherence could also cause a similar effect: if the bulk cross-sectional structure of the coronal hole is not preserved across altitude, then a low correlation should be expected between the low-altitude referent image and the topmost images from each instrument's useful range. By taking the referent from the top of the useful EIT range (at 1.18 $R_\odot$), Figure 5 demonstrates that the S/N is the main cause of the reduced peak height. The left-hand panel of Figure 5 shows cross-correlations between sinograms prepared identically to those in Figure 4*a* but with the referent at 1.18 $R_\odot$, the top of the considered altitude range for EIT. Except for the correlation spike for self-correlation, the higher altitude

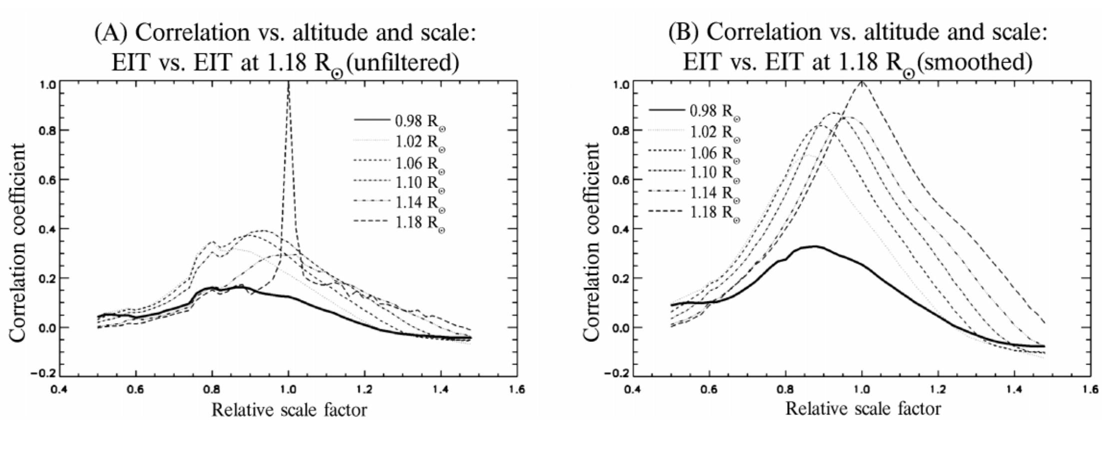

FIG. 5.—EIT sinogram cross-correlation coefficient across altitude and superradial expansion factor, showing that spatial decoherence is a minor effect for the data set plotted in Fig. 4. (*a*) Unfiltered sinograms. Because the image signal is weaker at higher altitudes, the S/N drops and so does the correlation peak. (*b*) Filtered sinograms. Smoothing the data over 3 × 3 pixel bins and rejecting outlying pixels reduces the noise level enough that the spatial coherence signal is visible in the correlation plots.

peaks are still weaker than the lower altitude peaks. Spatial decoherence would work in the opposite direction, causing the higher altitude sinograms to correlate better with the high-altitude reference image.

The right-hand panel of Figure 5 is the same plot after more thorough despiking and after smoothing with a 3 pixel FWHM circular Gaussian kernel to reduce the effects of the shot noise while not changing the overall spatial structure too much. The measured expansion ratios are the same as at left, but the correlation trend is toward higher correlation for closer sinograms, indicating that spatial decoherence is now more important to the correlation than is the specific noise level. The effects of noise are especially strong in the C1 data because they have the lowest S/N of the four channels.

3.5. *Long Vertical Extent of Features*

Because of the difficulty of tracking individual imaged structures across instruments' fields of view from the inner corona to the middle corona, there has been justifiable concern that the polar plumes that are visible in EIT data may not be the same structures as the rays that are visible in the LASCO data higher up (Llebaria et al. 1998). Individual studies that have linked plumes and rays (e.g., DeForest et al. 1997) using single montage images are convincing to some, but not all, readers. Llebaria et al. (1998), in particular, argued that the differences between sinograms assembled with EIT data and with LASCO C-2 data are likely caused by the instruments looking at different features. We quantified that concern by cross-correlating the EIT and LASCO sinograms at 1.06 and 2.39 $R_{\odot}$, respectively. Figure 6 is a similar diagram to the ones in Figure 4, showing that there is no significant correlation peak between those two altitudes and instruments at any reasonable scale factor.

Because the C-1 instrument can image both collisionally excited line emission (like EIT) and scattered photospheric continuum (like LASCO), it bridges the two different types of measurement. The C-1 instrument overlaps in altitude range with EIT and therefore must image the same coronal structures as EIT does. The C-1 continuum images measure integrated density and are insensitive to temperature, similarly to the LASCO C-2 data.

Figure 7 shows a similar diagram to the ones in Figure 4 but with cross correlation between two different instruments, C-2 and the C-1 continuum measurement, both of which measure integrated density and are insensitive to temperature. The solid line shows the correlation curve between the two sinograms, showing a well-defined peak at a scale factor of ~ 1.7. The low peak correlation coefficient of only 0.3 is largely due to the low S/N in the C-1 continuum signal; even between adjacent altitudes in LASCO C-1, the peak correlation signal is only 0.4. Hence, the structures within the coronal hole must have substantially the same cross section at both the lower and the upper altitude to support even the measured coefficient of 0.3 between the instruments.

3.6. *No Radial Component*

None of the panels in Figure 4 shows a significant radial component to the corona. If a significant fraction of the observed structures were to expand radially, as has been suggested by Woo et al. (1999), then there should be a significant correlation peak in each plotted curve at a scale Figure factor near 1.0. No such peak is visible in any of the

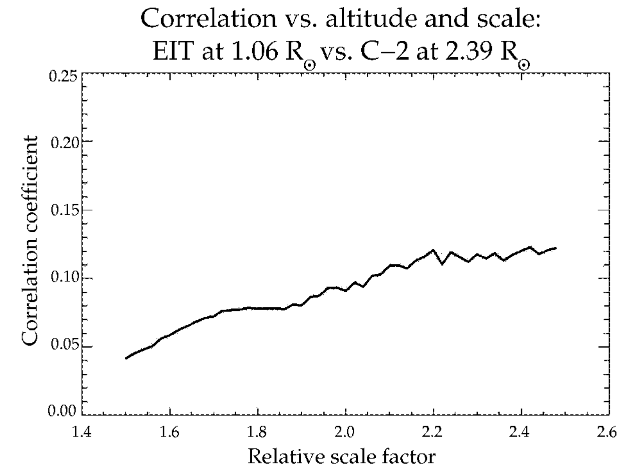

FIG. 6.—Sinogram cross-correlation coefficient between the lower corona (1.06 $R_{\odot}$) and mid-corona (2.39 $R_{\odot}$) as seen by EIT and LASCO C-2, respectively. The relatively weak cross-correlation coefficient, which reflects the different appearance of panels Figs. 3*a* and 3*b*, is due principally to the difference in measurement type and not to an incoherent expansion in the corona.

4 plots, indicating that there is no visible, radially expanding component to the coronal hole.

To test the strength of this null measurement, we generated hypothetical C-2 sinogram images with a small radial signal injected into the original data and cross-correlated them with the C-1 continuum sinogram at 1.18 $R_{\odot}$. The correlation curves are plotted along with the actual data in Figure 7. The injected radial signal is the C-1 continuum sinogram at 1.26 $R_{\odot}$, scaled to match the different azimuthal pixel size of the C-2 sinogram. It produces a peak at a relative expansion of 1.08. The peak is also visible in Figure 4*d*, which compares directly the 1.18 and 1.26 $R_{\odot}$ C-1 signals.

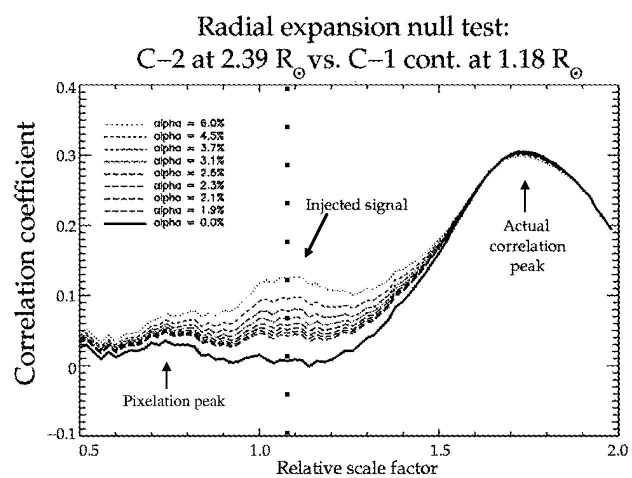

FIG. 7.—Sinogram cross-correlation coefficient between the lower corona (1.18 $R_{\odot}$) and midcorona (2.39 $R_{\odot}$) as seen by LASCO C-1 and C-2, respectively, both original data and hypothetical data with an added radial component. The solid line shows the cross-correlation curve using actual LASCO C-2 data. There is no significant peak at scales near 1.0. The dotted and dashed curves show the depth of the null measurement; even a small added signal with nearly radial expansion produces a significant peak (see text). Pixelation of the original data causes a small noise peak at a scale of 0.75.

A subsidiary peak is visible in Figure 7 at an expansion factor of 0.75. This small peak is due to the scaling of individual pixels; the horizontal pixel scale of the C-1 sinograms is $\frac{3}{4}$ of the horizontal scale of the C-2 sinograms, so that a scale factor of 0.75 brings individual pixel boundaries into alignment to produce a small correlation peak. This "pixelation peak" is a useful fiducial to indicate whether a small correlation peak is significant.

The injected sinogram was scaled to have the same rms value as the C-2 2.39 $R_\odot$ sinogram, then reduced by a variable factor a and added to the C-2 sinogram. The α-values shown on the plot represent the percentage of the total signal that is injected C-1 data: $\alpha^{-1} = 1 + a^{-1}$. We have plotted curves for values of α between 0% and 6% of the total signal. The 1.26 $R_\odot$ curve in Figure 4*d* is the equivalent curve for $\alpha = 0$.

Even for small values of α, there is a significant change in the shape of the correlation curve at the appropriate expansion factor of ~ 1.08. When 3.7% of the total signal is from the nearly radial source, the resulting nearly radial correlation peak is twice the height of the pixelation peak at the left. Furthermore, only approximately half of the C-1 continuum signal is solar in origin; the rest is local noise, as evidenced by the low cross-correlation coefficient between 1.18 and 1.26 $R_\odot$ in Figure 4*d*. We conclude that if even 2% of the total mass in the coronal hole were in differentiated, radially aligned structures, then we would resolve it in the shape of the solid line plot. Even a 2% injected signal (corresponding to a $\sim 1\%$ mass signal) is sufficient to produce a marginal detection with a height equal to the pixelation peak. No more than 1%–2% of the material in this coronal hole, by time-averaged mass, expanded radially with altitude.

3.7. *Form of the Superradial Expansion*

We used the peak locations in several cross-correlation curves, such as are shown in Figures 4–7, to produce an overall expansion profile for the coronal hole. This is a global measurement of the overall expansion factor $f_g(r)$ because the single expansion parameter fit is insensitive to uncorrelated expansion of individual features [the $f_l(r)$ used by Munro & Jackson 1977]. Each instrument or pair of instruments yields relative expansion factors between set ranges of altitudes. We used the EIT measurements to fix the expansion factor at 1.18 $R_\odot$, which is visible in three of the four instrument channels in Figure 4. The C-2 expansion factors were determined by cross-correlation with the C-1 continuum 1.18 $R_\odot$ signal (in Fig. 7), allowing absolute calibration to be transferred back to the EIT signal (which includes 1.0 $R_\odot$).

Figure 8 shows an assembled plot of superradial expansion, based on seven comparison suites. In general, different instrument suites yielded good agreement in the superradial expansion coefficient. A notable exception was the high range of LASCO C-1 altitudes in which the S/N was particularly low. The line and continuum C-1 measurements diverge slightly above 1.3 $R_\odot$ by about 5%. The upper altitude coefficients are anchored by the C-1 continuum 1.18 $R_\odot$ measurement, in which the C-1 S/N is largest in both channels.

Figure 8 plots the global expansion coefficient $f_g(r)$ of the coronal hole as a whole rather than the local expansion coefficient $f_l(r)$ of individual features (Suess et al. 1998). The measured expansion coefficients—1.5 at ~ 1.5 $R_\odot$ and 2.25 at ~ 3 $R_\odot$—are consistent with measurements by DeForest et al. (1997) and Cranmer et al. (1999) but slightly slower than other expansion factors such as those found by Guhathakurta et al. (1999), Guhathakurta & Holzer (1994), and Munro & Jackson (1977). Our maximum measured expansion factor of 2.25 should not be construed as a maximum total expansion; the corona continues to expand superradially until $\sim$4–5 $R_\odot$ (see, e.g., Munro & Jackson 1977; DeForest et al. 1997). We have not continued the analysis to that altitude range because the C-2 polar data were truncated at just over 3 $R_\odot$ until later in the *Solar and Heliospheric Observatory* (*SOHO*) mission. Later data include more interference because of low-latitude streamers as solar cycle 23 progressed.

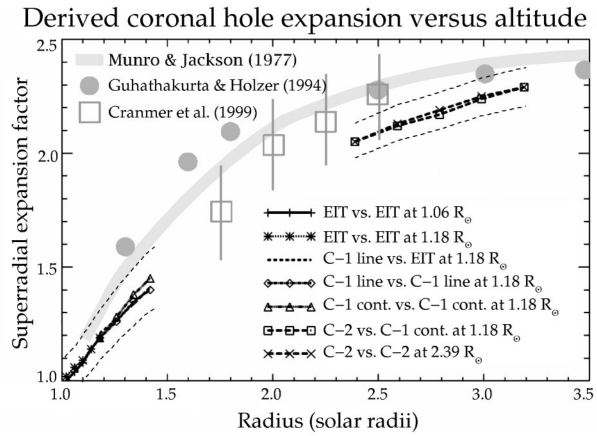

FIG. 8.—Superradial expansion of the lower coronal hole determined by sinogram cross-correlation. The structural signature contained in the sinograms allows accurate measurement of expansion even across the 1.3–2.4 $R_\odot$ gap in instrument availability. The dashed error envelope lines reflect the average FWHM of the correlation curves from which the expansion ration is derived, although the close agreement between different sinogram pairs shows that the expansion ratio measurement is much more precise. Expansion factors from Guhathakurta & Holzer (1994), DeForest et al. (1997), and Cranmer et al. (1999) are plotted for comparison. See text for caveats.

The slightly lower trend in the Figure 8 expansion factors, compared to the other expansion curves in the literature, arises from the fact that all of the other curves shown are derived from the edges of the observed coronal holes, while our curve is derived from expansion of the center of the coronal hole. While the expansion factor is here modeled as uniform throughout the coronal hole, the trend of the observed feature misalignments in Figure 3 shows that structures near the center of the coronal hole tend to expand slightly more slowly than structures that are closer to the edge, suggesting that our measurements of the core of the coronal hole are biased slightly toward lower expansion coefficients compared to observations of the edges.

4. CONCLUSIONS

We have further developed a projection technique that is useful for understanding both time dependence and spatial variations of the coronal hole structure, as also demonstrated by Lamy et al. (1997) and Li et al. (2000). We have used the technique to determine the expansion rate of solar minimum polar coronal holes, to demonstrate that there is no radial component to solar minimum polar coronal holes, and to determine the form of the superradial expansion coefficient $f_g(r)$. In addition, we are able to track (in at least a rudimentary way) the evolution and life cycle of polar plumes, features that have so far been difficult to track in EUV movies of the solar minimum coronal holes.

Our expansion analysis relies on resolution of individual, tall structures at various altitudes in the corona; we have cross-correlated the spatiotemporal pattern that is formed by the rotation and evolution of polar plumes and other coronal hole structures. Because the cross-correlation technique removes the human element in image interpretation, its results are more credible than simple image alignment studies using the same types of data (DeForest et al. 1997; Woo et al. 1999). We find that there is no significant component of the coronal hole that expands radially and coherently with altitude; any radial structures must either account for under 1% of the coronal hole by mass or be shorter than $\sim 1\ R_{\odot}$ in height.

From the feature alignments in Figure 3, it is clear that the cross-sectional morphology of the corona changes slightly with altitude so that a simple one-parameter $f_g(r)$ scaling is not sufficient to describe fully the coronal hole's expansion. While the single parameter describes the expansion well to perhaps a 5%–10% level, further precision requires more parameters to the fit. Second-order models of coronal expansion must include at least a latitudinal dependence to the expansion factor and a possible helical component to the coronal hole's structure. Both of these extensions would require at least rudimentary tomographic interpretation of the results. In the current work, we have used the happy coincidence that simple scaling has the same functional form in one dimension (in the sinograms) as in two (in the original coronal cross section) to avoid any requirement for tomographic interpretation of the results.

Our expansion factors may be used to constrain coronal hole models. For example, of the three models discussed in Suess et al. (1998), only the Wang et al. (1995) model well approximates the expansion curve shown in Figure 8.

There is no particular reason why the techniques we outline here cannot be extended to higher altitudes or to fill in the altitude gap between ~ 1.5 and $\sim 2.5\ R_{\odot}$. In particular, the High Altitude Observatory Mk 3 coronameter (Fisher et al. 1981) is well suited to the lower altitude range and the LASCO C-3 instrument to the higher one. Future work should include measurements of $f_g(r)$ over the full available range of altitudes.

C. E. D. was supported for this work by NASA grants NAG 5-9795 and NSG 5131. Special thanks to the SOI/MDI team. P. L. L. and A. L. are supported by CNRS and CNES. EIT data are courtesy of the EIT consortium. We are indebted to Rainer Schwenn, Russ Howard, Dennis Socker, and John Cook at the Naval Research Laboratory for indispensable help in understanding the C-1 data and to Joe Davila at NASA's Goddard Space Flight Center for valuable discussions on tomography and for introducing to us the term "sinogram." *SOHO* is a project of international collaboration between ESA and NASA.

REFERENCES

Banerjee, D., Teriaca, L., Doyle, J. G., & Lemaire, P. 2000, Sol. Phys., 194, 43
Brueckner, G. E., et al. 1995, Sol. Phys., 162, 357
Cranmer, S. R., et al. 1999, ApJ, 511, 481
DeForest, C. E., Hoeksema, J. T., Gurman, J. B., Thompson, B. J., Plunkett, S. P., Howard, R., Harrison, R. C., & Hasslerz, D. M. 1997, Sol. Phys., 175, 393
DeForest, C. E., Plunkett, S. P., & Andrews, M. D. 2001, ApJ, 546, 569
Delaboudiniére, J. P., et al. 1995, Sol. Phys., 162, 291
Fisher, R., & Guhathakurta, M. 1995, ApJ, 447, L139
Fisher, R. R., Lee, R. H., MacQueen, R. M., & Poland, A. I. 1981, Appl. Opt., 20, 1094
Giordano, S., Antonucci, E., Noci, G., Romoli, M., & Kohl, J. L. 2000, ApJ, 531, L79
Guhathakurta, M., Fludra, A., Gibson, S. E., Biesecker, D., & Fisher, R. 1999, J. Geophys. Res., 104, 9801
Guhathakurta, M., & Holzer, T. E. 1994, ApJ, 426, 782
Hassler, D. M., Dammasch, I. E., Lemaire, P., Brekke, P., Curdt, W., Mason, H. E., Vial, J.-C., & Wilhelm, K. 1999, Science, 283, 810
Lamy, P., et al. 1997, in The Corona and Solar Wind Near Minimum Activity, ed. A. Wilson (ESA SP-404; Noordwijk: ESA), 487
Li, J., Jewitt, D., & LaBonte, B. 2000, ApJ, 539, L67a
Li, J., Kuhn, J., LaBonte, B., Raymond, J. C., & Acton, L. W. 2000b, ApJ, 538, 415
Llebaria, A., Lamy, P. L., DeForest, C. E., & Koutchmy, S. 1998, in Solar Jets and Coronal Plumes, ed. T. D. Guyenne (ESA SP-421; Noordwijk: ESA), 87
McComas, D. J., Barraclough, B. L., Gosling, J. T., Hammond, C. M., Phillips, J. L., Neugebauer, M., Baloh, A., & Forsythe, R. J. 1995, in Solar Wind Eight, ed. D. Winterhalter (Woodbury: AIP), 44
Munro, R. H., & Jackson, B. V. 1977, ApJ, 213, 874
Newkirk, G., & Harvey, J. 1968, Sol. Phys., 3, 321
Poletto, G., Parenti, S. Noci, G. Livi, S. Suess, S. T. Balogh, A. & McComas, D. J. 1996, A&A, 316, 374
Reisenfeld, D. B., McComas, D. J. & Steinberg, J. T. 1999, Geophys. Res. Lett., 26, 1805
Saito, K. 1965, PASJ, 17, 1
Schrijver, C. J., Title, A. M., van Ballegooijen, A. A., Hagenaar, H. J., & Shine, R. A. 1997, ApJ, 487, 424
Suess, S. T., Poletto, G., Wang, A.-H., Wu, S. T., & Cuseri, I. 1998, Sol. Phys., 180, 231
Wang, Y.-M. 1994, ApJ, 435, L153
———. 1998, ApJ, 501, L145
Wang, Y.-M., & Sheeley, N. 1995, ApJ, 452, 457
Wang, A.-H., Wu, S. T., Suess, S. T., & Poletto, G. 1995, Sol. Phys., 161, 365
Withbroe, G. L., Feldman, W. C., & Ahluwalia, H. S. 1991, in Solar Interior and Atmosphere, ed. A. N. Cox & H. S. Matthews (Tucson: Univ. Arizona Press), 1087
Woo, R., & Habbal, S. 1999, ApJ, 510, L69
Woo, R., Habbal, S. R., Howard, R. A., & Korendyke, C. M. 1999, ApJ, 513, 961
Wu, S. T., et al. 1997, Sol. Phys., 175, 719
Zirker, J. B., ed. 1977, Coronal Holes and High Speed Wind Streams (Boulder: Univ. Colorado Press)